



**HAL**  
open science

## Trapped and Leaking Energetic Particles in Injection Flux Tubes of Saturn's Magnetosphere

Ze-Fan Yin, Yi-Xin Sun, Xu-Zhi Zhou, Dong-Xiao Pan, Zhong-Hua Yao, Chao Yue, Ze-Jun Hu, Elias Roussos, Michel Blanc, Hai-Rong Lai, et al.

► **To cite this version:**

Ze-Fan Yin, Yi-Xin Sun, Xu-Zhi Zhou, Dong-Xiao Pan, Zhong-Hua Yao, et al.. Trapped and Leaking Energetic Particles in Injection Flux Tubes of Saturn's Magnetosphere. *Geophysical Research Letters*, 2023, 50, 10.1029/2023GL105687 . insu-04473144

**HAL Id: insu-04473144**

**<https://insu.hal.science/insu-04473144>**

Submitted on 23 Feb 2024

**HAL** is a multi-disciplinary open access archive for the deposit and dissemination of scientific research documents, whether they are published or not. The documents may come from teaching and research institutions in France or abroad, or from public or private research centers.

L'archive ouverte pluridisciplinaire **HAL**, est destinée au dépôt et à la diffusion de documents scientifiques de niveau recherche, publiés ou non, émanant des établissements d'enseignement et de recherche français ou étrangers, des laboratoires publics ou privés.



Distributed under a Creative Commons Attribution 4.0 International License

# Geophysical Research Letters<sup>®</sup>



## RESEARCH LETTER

10.1029/2023GL105687

Ze-Fan Yin and Yi-Xin Sun contributed equally to this work.

### Key Points:

- In Saturn's injection flux tubes, charged particles often show distinct energy-dispersive or dispersionless signals depending on pitch angle
- The unexpected, energy-dispersionless features for perpendicular-moving particles are formed by their trapping motion within the flux tubes
- The bouncing particles can hardly be trapped, and therefore, exhibit the characteristic energy dispersion and particle leaking signatures

### Correspondence to:

X.-Z. Zhou,  
[xzzhou@pku.edu.cn](mailto:xzzhou@pku.edu.cn)

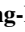


### Citation:

Yin, Z.-F., Sun, Y.-X., Zhou, X.-Z., Pan, D.-X., Yao, Z.-H., Yue, C., et al. (2023). Trapped and leaking energetic particles in injection flux tubes of Saturn's magnetosphere. *Geophysical Research Letters*, 50, e2023GL105687. <https://doi.org/10.1029/2023GL105687>

Received 27 JUL 2023

Accepted 26 SEP 2023

## Trapped and Leaking Energetic Particles in Injection Flux Tubes of Saturn's Magnetosphere

Ze-Fan Yin<sup>1,2</sup> , Yi-Xin Sun<sup>1</sup> , Xu-Zhi Zhou<sup>1</sup> , Dong-Xiao Pan<sup>3</sup> , Zhong-Hua Yao<sup>4</sup> , Chao Yue<sup>1</sup> , Ze-Jun Hu<sup>2</sup> , Elias Roussos<sup>5</sup> , Michel Blanc<sup>6</sup> , Hai-Rong Lai<sup>7</sup> , and Qiu-Gang Zong<sup>1</sup> 

<sup>1</sup>School of Earth and Space Sciences, Peking University, Beijing, China, <sup>2</sup>MNR Key Laboratory for Polar Science, Polar Research Institute of China, Shanghai, China, <sup>3</sup>School of Geophysics and Information Technology, China University of Geosciences, Beijing, China, <sup>4</sup>Key Laboratory of Earth and Planetary Physics, Institute of Geology and Geophysics, Chinese Academy of Sciences, Beijing, China, <sup>5</sup>Max Planck Institute for Solar System Research, Göttingen, Germany, <sup>6</sup>Institut de Recherche en Astrophysique et Planétologie, Toulouse, France, <sup>7</sup>School of Atmospheric Sciences, Sun Yat-sen University, Zhuhai, China

**Abstract** In Saturn's magnetosphere, the radially-inward transport of magnetic fluxes is usually carried by localized flux tubes with sharply-enhanced equatorial magnetic fields. The flux tubes also bring energetic particles inward, which are expected to drift azimuthally and produce energy-dispersive signatures. Spacecraft observations, however, indicate the occurrence of energy-dispersionless signatures for perpendicular-moving particles. These unexpected features are attributed to the sharp magnetic gradient at the edge of the flux tubes, which significantly modifies the drift trajectories of perpendicular-moving particles to enable their trapping motion within the flux tubes. The bouncing particles are less affected by the gradient, and therefore, still display energy-dispersive signatures. It is the distinct particle behavior, together with different spacecraft traversal paths, that underlies the observational diversity. The results improve our understanding of particle dynamics in the magnetospheres of giant planets and indicate that pitch-angle information should be considered in the extraction of flux-tube properties from energetic particle observations.

**Plain Language Summary** The conservation of magnetic fluxes in Saturn's magnetosphere requires that the outward convection is compensated by a return process of magnetic fluxes, which has been observed in the form of localized flux tubes associated with sharply-enhanced equatorial magnetic field and hot plasma population. The azimuthal drift of energetic particles within the flux tubes produces energy-dispersive signatures, which have been utilized to estimate the age and starting position of the returning flux tubes. In this paper, we are motivated by Cassini observations of energy-dispersionless signatures for perpendicular-moving particles, to demonstrate that their drift paths can be significantly modified by the sharp magnetic gradient to cause their trapping within the flux tubes. The bouncing particles, on the other hand, are less affected by the gradient and, therefore, can leave the flux tubes to continue their drift around the planet. We further construct the magnetic configuration associated with the flux tubes, to illustrate the origin of the diverse observational signatures depending on particle pitch angle, spacecraft traversal path, and the trapping extent. These results have important implications for the interpretation of observational data in the injection flux tubes, and therefore improve our understanding of giant planet's magnetosphere and the associated particle dynamics.

## 1. Introduction

Saturn's magnetosphere is a rapidly-rotating system with dominant plasma sources in the inner magnetosphere (Blanc et al., 2015; Mauk et al., 2009; Thomsen, 2013, and references therein). The cold plasmas originating from the ionization of the Enceladus plumes are transported outward by centrifugal force before their eventual loss to the solar wind (Vasyliunas, 1983). The outward motion is also associated with outward transport of magnetic fluxes, which must be compensated by an inward flux return. The returning fluxes are usually observed in the form of localized flux tubes characterized by the sudden appearance of a hot, tenuous population replacing the cold, dense plasmas (Burch et al., 2005; Hill et al., 2005; Rymer et al., 2009). The concomitant magnetic measurements often exhibit an enhanced magnitude near the equator, although the magnitude is reduced at higher latitudes outside the plasma disk (André et al., 2005, 2007; Lai et al., 2016). Based on these signatures, many injection flux tubes have been identified observationally (Azari et al., 2018; Lai et al., 2016; Paranicas et al., 2020; Yao et al., 2017).

© 2023. The Authors.

This is an open access article under the terms of the [Creative Commons Attribution License](https://creativecommons.org/licenses/by/4.0/), which permits use, distribution and reproduction in any medium, provided the original work is properly cited.

This process takes place on both nightside and dayside (Delamere et al., 2015; Guo et al., 2018), and the plasma transport in the rotating magnetosphere is along both radial and azimuthal directions.

The formation of the injection flux tubes has yet to be fully understood. A relatively-established scenario is based on interchange instability (Hill et al., 2005; Liu et al., 2010; Mauk et al., 2009), during which the outside (hot) and inside (cold) plasmas are interchanged at the outer edge of the plasma torus. The interchange occurs because the cold dense plasma overlies the hot tenuous population, with the role of gravity in Rayleigh-Taylor instability replaced by the centrifugal force. Thomsen et al. (2015) proposed that the hot plasma from nightside reconnection would be separated from the cold, inner-magnetospheric population by a sharp boundary at dipole L-shell of  $\sim 9$ , where interchange occurs. An alternative mechanism is that the depleted flux tubes (after the down-tail mass unloading) can return directly to the inner magnetosphere, which is supported by similar flux-tube properties across a wide radial distance without a clear boundary separation (Lai et al., 2016). This evidence did not stop the debate, however. According to Thomsen and Coates (2019), the statistical results could be alternatively explained by dynamic variations of the boundaries.

To differentiate the two mechanisms, many studies have attempted to derive the age and starting position of the injection flux tubes based on energy dispersion of particles observed therein (Chen & Hill, 2008; Hill et al., 2005; Lai et al., 2021; Paranicas et al., 2016). The dispersion originates from the energy dependence of magnetic gradient and curvature drift velocities, which are in the same direction as the flux-tube corotation (anticlockwise) for ions but opposite (clockwise) for electrons. Therefore, ions with higher energies and electrons with lower energies would drift faster around the planet, which indicates that the high-energy cutoffs of ion and electron fluxes in the observed energy-time spectrograms would decrease and increase over time, respectively (Burch et al., 2005). The energy-dispersive signatures thus provide important information on flux-tube properties, which could be extracted by tracing the energetic particles backward in time to the starting positions without energy dispersion (e.g., Hill et al., 2005; Lai et al., 2021).

The energy-dispersive signatures discussed above are not universal, however. It has been shown in Mitchell et al. (2015) that in certain events, the observed energy dispersion could be distinctly different for particles with different pitch angles. We aim to understand this phenomenon in this study. Based on Cassini observations, we demonstrate that the pitch-angle dependence of particle dispersion originates from the sharp magnetic gradient at the edge of the injection flux tubes, which enables the trapping of equatorially-mirroring particles to form energy-dispersionless signatures. The bouncing particles with pitch angles closer to  $0$  or  $180^\circ$ , on the other hand, are hardly affected by the sharp gradient, and they still display the characteristic energy dispersion. These results improve our understanding of energetic-particle dynamics in Saturn's magnetosphere and suggest that pitch-angle information should be considered in the extraction of flux-tube properties from the observations of energy dispersion.

## 2. Observations

Several Cassini instruments are used in this study. The magnetic measurements are provided by the Cassini magnetometer (Dougherty et al., 2004) with a 1-s data resolution. The CHarge Energy Mass Spectrometer (CHEMS) in the Magnetosphere Imaging Instrument (MIMI) suite (Krimigis et al., 2004) detects energetic ions of  $\sim 3$ – $220$  keV/e with distinguishable composition by three telescopes pointing to different elevation angles. The Electron Spectrometer (ELS; Linder et al., 1998) in the Cassini Plasma Spectrometer (CAPS; Young et al., 2004) measures electron distributions below  $\sim 28$  keV via eight elevation anodes. Although CHEMS and CAPS only cover a limited field of view, it is still possible to measure the fluxes of equatorially-mirroring and bouncing particles simultaneously, especially when Cassini is near the equator with the background magnetic field approximately along the Z-axis of the spacecraft.

The left column of Figure 1 shows Cassini observations of an injection flux tube near the equator (latitude  $\sim 0.3^\circ$ ) on 21 March 2006 (referred to as Case I hereafter), which are characterized by a sharp enhancement of the magnetic strength (Figure 1b) and the sudden appearance of hot plasmas (Figures 1c–1k). The leading and trailing edges of the flux-tube traversal are given by vertical dashed lines in Figure 1, at  $\sim 05:16:00$  UT and  $\sim 05:23:30$  UT, respectively. Based on the orientations of the three CHEMS telescopes, we show in Figure 1c–1e the energy-time spectrograms of the differential energy fluxes (DEF) for energetic protons with different pitch angles, of  $\sim 38^\circ$ ,  $\sim 91^\circ$ , and  $\sim 144^\circ$ , respectively. The pitch angles correspond to the field-of-view center for each telescope, which vary by  $< 2^\circ$  during the 20-min interval. Obviously, the energy spectrograms for bouncing protons ( $\sim 38^\circ$  and

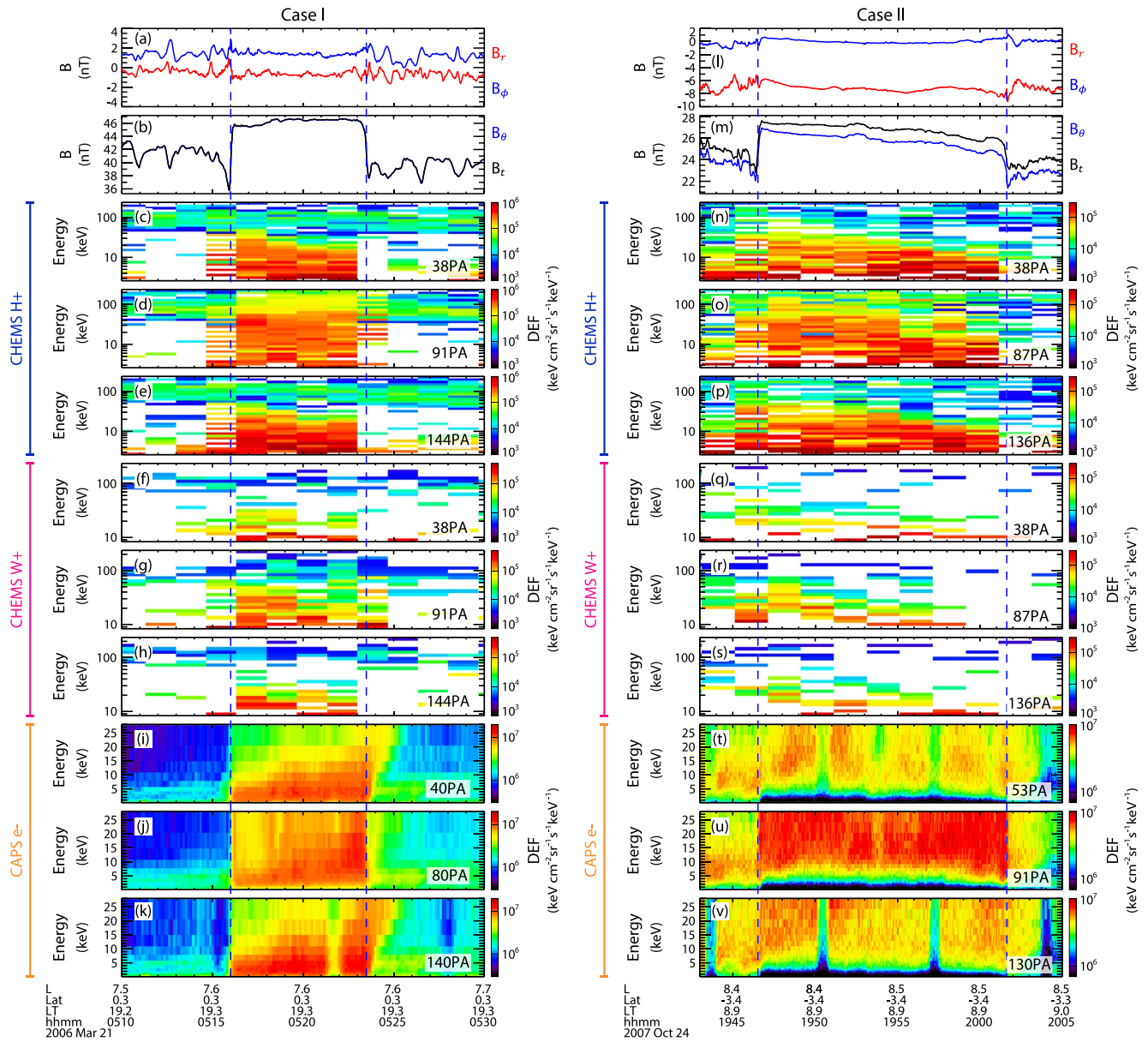


**Figure 1.** Cassini observations of injection flux tubes on 21 March 2006 (left, Case I) and 24 October 2007 (right, Case II). The observations for Case I include: (a) radial (red) and azimuthal (blue) components of the magnetic field; (b) polar component (blue) and the strength (black) of the magnetic field (nearly overlapped); (c)–(e) energy-time spectrograms of differential energy fluxes (DEF) for energetic protons measured by three CHEMS telescopes, corresponding to different pitch angles given in the lower-right corners; (f)–(h) water-group ion observations in the same format as in (c)–(e); (i)–(k) energy-time spectrograms of the electron DEF from different CAPS-ELS anodes with different pitch angles. The vertical dashed lines mark the leading and trailing edges of the flux-tube traversal, respectively. The observations for Case II, shown in the right column (l)–(v), are in the same format as in the left column.

~144°) display energy-dispersive signatures with decreasing high-energy cutoffs within the flux tube (between two vertical lines, see Figures 1c and 1e). By contrast, the high-energy cutoffs of the perpendicular-moving protons remain at higher levels without clear energy dispersion (compare Figures 1d to 1c and 1e). These observations imply different behavior of protons with different pitch angles, which will be analyzed in the next section. We also show in Figures 1f–1h the energy spectrograms of water group ions (W<sup>+</sup>, including H<sub>2</sub>O<sup>+</sup>, OH<sup>+</sup>, and O<sup>+</sup>). Like the protons, the bouncing W<sup>+</sup> ions also exhibit energy-dispersive features (Figures 1f and 1h), whereas the signatures for equatorially-mirroring W<sup>+</sup> ions are nearly dispersionless (Figure 1g).

The pitch-angle dependence of energetic-electron observations, revealed by different CAPS-ELS anodes, is shown in Figures 1i–1k. Here, we display measurements from anode 2, a mean value of anodes 4 and 5, and

anode 7, which correspond to the pitch angles of  $\sim 40^\circ$ ,  $\sim 80^\circ$  ( $\sim 100^\circ$ ), and  $\sim 140^\circ$ , respectively. The pitch angles for each anode are stable with the variation range of  $\sim 5^\circ$ . The energy-time spectrograms exhibit characteristic energy dispersion for bouncing electrons within the flux tube (Figures 1i and 1k), with higher-energy electrons being observed later. The perpendicular-moving electrons, on the other hand, show abrupt flux enhancements simultaneously across a wide energy range. After Cassini departs from the flux tube (the second dashed line), the energy-dispersive flux reduction can still be observed for bouncing electrons (Figures 1i and 1k), although the dispersion slope is steeper than that within the flux tube. By contrast, the perpendicular-moving electrons display nearly-simultaneous reduction at all energy channels (Figure 1j). In other words, the flux-tube leakage occurs only for particles mirroring far from the equator.

Case I is only an example with pitch-angle dependent signatures in energy dispersion. There are counter-examples, too. The right column of Figure 1 shows another flux-tube traversal on 24 October 2007 (in the same format as the left column, referred to as Case II), in which energy dispersion occurs for both perpendicular-moving and bouncing particles. The leading and trailing edges of the flux-tube traversal, marked by vertical lines in Figures 1l–1v, are at  $\sim 19:46:30$  UT and  $\sim 20:01:37$  UT, respectively. Obviously, the perpendicular-moving (Figure 1o) and bouncing protons (Figures 1n and 1p) both exhibit energy-dispersive features within the flux tube, with higher-energy protons being detected earlier. Similar dispersive features also apply to water-group ions (Figures 1q–1s) despite their lower fluxes. Unfortunately for this event, the dispersion signatures cannot be resolved for electron measurements due to the limited energy range (Figures 1t–1v). Also, the two sudden drops of electron fluxes in Figures 1t and 1v are artificial due to the field-of-view obscuration by other Cassini constituents (see Figure 5 in Young et al. (2004)).

The different signatures between Cases I and II, especially in that the fluxes of equatorially-mirroring ions could be either energy-dispersionless (as in Case I) or energy-dispersive (Case II), are to be analyzed below. We mainly focus on the field perturbations and spacecraft trajectories with respect to the flux tubes.

### 3. Analysis

To obtain properties of an injection flux tube (such as its size and the magnitude of magnetic perturbations), it is important to quantitatively determine the leading and trailing edges of the spacecraft traversal. We first follow the Yin et al. (2022) procedure to calculate the  $n$ -point binomial-weighted average of the field strength within a 10-s window and derive its rate of change  $\Delta B/\Delta t$ . The leading and trailing edges are then determined by the time of maximum and minimum  $\Delta B/\Delta t$ , labeled as  $t_0$  and  $t_1$ , respectively (the vertical lines in Figure 1). Taking the leading edge as an example, we determine the maximum and minimum values of the field strength within  $t_0 \pm 15$  s, as the magnetic field immediately inside and outside the tube. The difference between them,  $\delta B_0$ , represents the field enhancement across the leading edge. The corresponding time difference,  $\delta t_0$ , represents the crossing duration of the leading-edge boundary. The  $\delta B_1$  and  $\delta t_1$  values for the trailing edge are determined similarly. We then treat the average value  $\delta B = (\delta B_0 + \delta B_1)/2$  as the magnitude of the field perturbations across the flux tube, which are 9.15 and 3.62 nT for Cases I and II, respectively. Since the perturbed field is predominantly in the  $\theta$  direction (see Figures 1a–1b and 1l–1m), the  $\delta B$  values are approximately the magnitude of  $B_\theta$  variations. The boundary-crossing durations,  $\delta t_0$  and  $\delta t_1$ , are  $\sim 20$  s for both events.

The flux-tube size estimation is more difficult. For each flux tube, we perform the minimum variance analysis (MVA; Sonnerup & Scheible, 1998) to determine the normal directions of the leading and trailing edges. Taking the leading edge as an example, we continuously adjust the width of the MVA window (ranging from  $\delta t_0$  to  $2\delta t_0$ , in which the maximum and minimum field immediately inside and outside the tube must be covered), to determine the normal direction with maximum ratio between intermediate and minimum eigenvalues,  $\lambda_M/\lambda_N$ . The determined normal vectors in Kronographic Radial-Theta-Phi (KRTP) coordinates for the leading and trailing edges are  $\pm(0.9, 0.15, -0.41)$  and  $\pm(0.36, 0.02, -0.93)$  for Case I, and  $\pm(-0.58, -0.13, 0.81)$  and  $\pm(0.1, 0.14, 0.98)$  for Case II, respectively. The ratio  $\lambda_M/\lambda_N$  for these crossings are all greater than 10, indicating reliable determination of the normal directions. For each event, the angle between the leading- and trailing-edge normal directions contains important information on spacecraft trajectory across the flux tube, especially if we follow the Lai et al. (2016) statistics to assume circular cross-sections of the flux tube.

The normal directions determined via MVA, however, are subject to a  $180^\circ$  ambiguity. To resolve this ambiguity, we assume that the azimuthal propagation velocity of each flux tube is the same as the sub-corotation ion flow

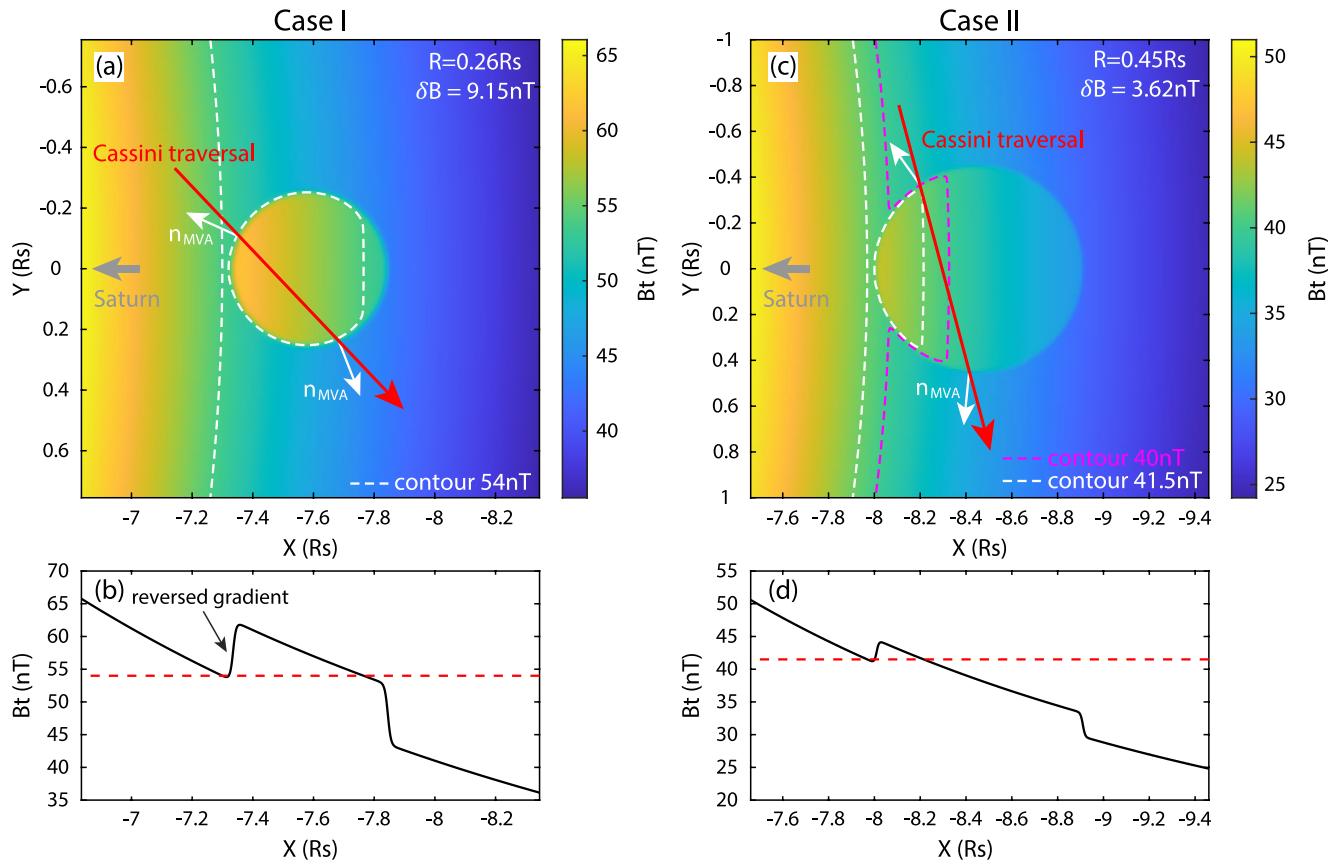


**Figure 2.** The estimated spacecraft trajectory in the flux-tube rest frame for Cases I (left) and II (right), respectively. (a) Equatorial distribution of the field strength (background color), with the white arrows illustrating normal directions across the edges, the red arrow marking the spacecraft trajectory, and the dashed lines representing field-strength contours. (b) Radial profile of field strength at  $y = 0$ , with the dashed line corresponding to the value of the white contour in panel (a). Panels (c)–(d) are in the same format as in (a)–(b).

(Wilson et al., 2009), and that the tube also undergoes a radially-inward motion. In other words, in the flux-tube rest frame, the spacecraft should traverse the tube in the westward and anti-planetward directions. The resolved normal directions (white arrows in Figure 2) are thus used to derive the spacecraft trajectory across the flux tube (red arrows in Figure 2), which can be combined with the sub-corotation speed (Wilson et al., 2009) to estimate the flux-tube size. The cross-section radii of the flux tubes are  $R = 0.26R_s$  (where  $R_s = 60268$  km is Saturn's radius) for Case I and  $R = 0.45R_s$  for Case II. An alternative assumption of rigid corotation would correspond to slightly larger flux-tube radii ( $0.36$  and  $0.63R_s$ , respectively), although the subsequent analysis is hardly affected by the minor uncertainties.

Figure 2 shows the estimated spacecraft traversal trajectory in the flux-tube rest frame for Cases I (left) and II (right), respectively. The spacecraft trajectory is marked by the red arrow, and the background color illustrates the equatorial field strength (which involves the background dipole and the localized perturbations). Here, the perturbed field is constructed based on a simple model with a circular boundary,

$$B_f = \frac{\delta B}{2} \left\{ 1 - \tanh \left[ \frac{\sqrt{(x-x_0)^2 + (y-y_0)^2} - R}{D} \right] \right\}, \quad (1)$$

where  $\delta B$  represents the field enhancements,  $R$  is the flux-tube radius,  $D$  is the half-thickness of the flux-tube edge ( $0.01R_s$ , consistent with the boundary crossing duration of  $\sim 20$  s), and  $x_0$  and  $y_0$  represent the tube's center location. This expression has been used to model the dipolarizing flux bundles in Earth's magnetotail (Zhou et al., 2014). The flux-tube motion in the spacecraft frame corresponds to an electric field through Faraday's law. In the flux-tube rest frame, however, the electric field perturbations are negligible. We also disregard the magnetic-local-time (MLT) of the flux tube, to simply put its center at  $y_0 = 0$  and  $x_0 < 0$  (with  $|x_0|$  equal to

the mean L-shell during the spacecraft traversal). We also display contours of the field strength for each event (dashed lines in Figures 2a and 2c) and the radial field-strength profiles along  $y = 0$  (Figures 2b and 2d). An important feature in Figure 2 is the presence of sharp, reversed magnetic gradients at the inner edge, which leads to closed contours of the magnetic strength within the flux tube (white dashed lines). It also illustrates a clear difference between Cases I and II, which lies in the spacecraft traversal trajectory with respect to the closed magnetic contours.

The drift motion of perpendicular-moving energetic particles, mainly controlled by the magnetic gradient drift, would be significantly modified by this field configuration. Based on the expression of magnetic gradient drift,

$$v_{\nabla} = \frac{\mu}{q\gamma} \frac{\mathbf{B} \times \nabla B}{B^2}, \quad (2)$$

where  $\mu$  is the particle's magnetic moment,  $q$  is the particle's charge,  $\gamma$  is the Lorentz factor and  $\mathbf{B}$  is the magnetic field, the drift motion is perpendicular to the magnetic field and its gradient (Baumjohann & Treumann, 1996). Given a southward field and a gradient perpendicular to the field-strength contour, an equatorially-mirroring particle would drift along the closed contour and be trapped inside the flux tube. Specifically, the ions (electrons) would drift westward (eastward) near the planetward edge but in opposite directions (eastward for ions and westward for electrons) at farther distances, to constitute the closed drift paths. The scenario of particle trapping is similar to the one for magnetic dips in Earth's magnetosphere (Yin et al., 2021). According to this scenario, the size of the trapping region is determined by the outermost, closed contour of field strength, where the abrupt, energy-dispersionless flux variations are expected for perpendicular-moving particles.

For bouncing particles with pitch angles near  $0^\circ$  or  $180^\circ$ , the drift motion is governed by magnetic curvature drift, which is hardly affected by the sharp magnetic gradient. Therefore, we can still expect their leakage from the flux tube and the typical, energy-dispersive signatures. At intermediate pitch angles, the particle motion near the edge is determined by a competition between magnetic gradient and curvature drift velocities in different directions. A quantitative comparison between them requires accurate information on the latitudinal profile of the field perturbations, which is unavailable in Equation 1 and unclear from spacecraft observations, although it is obvious that particles with pitch angles closer to  $90^\circ$  would more likely be trapped within the flux tube, and those closer to  $0$  or  $180^\circ$  would likely follow open trajectories.

As a result, when the spacecraft traverses the trapping region (Case I), it would observe distinct signatures for particles with different pitch angles (energy-dispersionless and dispersive for pitch angles closer to and far from  $90^\circ$ , respectively). For Case II, the spacecraft hardly traverses the trapping region (white contour in Figure 2c) and thus cannot observe the trapped population. In fact, the drift trajectories of perpendicular-moving particles outside the trapping region could extend outside the flux tube (magenta contour in Figure 2c), and their energy-dependent drift speed indicates the occurrence of energy dispersion in a similar fashion to the bouncing particles.

In other words, the diverse energetic-particle signatures depend on pitch angle and spacecraft traversal path with respect to the trapping region. Since a larger trapping region (or more precisely, a larger ratio of the trapping region to the entire flux tube) would enhance the possibility for a spacecraft to observe the pitch-angle dependence of dispersion signatures, we next examine the factors that determine this ratio. Consider a flux tube with field enhancement  $\delta B$ , radius  $R$  (in  $R_s$ ), L-shell  $L_0$  at its center, and for simplicity, an infinitely-sharp edge (with  $D$  approaching zero in Equation 1). The radial extent of the trapping region is determined by the location where the field strength equals to that immediately ahead of the inner edge (see the horizontal lines in Figures 2b and 2d). Let the trapping region extend to the farthest radial distance of  $L_0 - \delta R$  (with  $\delta R$  ranging from  $-R$  to  $R$ ), we have

$$\frac{B_s}{(L_0 - R)^3} = \frac{B_s}{(L_0 - \delta R)^3} + \delta B, \quad (3)$$

where  $B_s = 21,000$  nT is the equatorial field strength at Saturn's surface. Since the tube radius  $R$  (typically below  $\sim 0.5R_s$ ) is much smaller than its L-shell (above  $5R_s$ ), we apply a first-order Taylor approximation on Equation 3, to derive the ratio  $\alpha$  of the trapping region to the flux tube in the radial direction,

$$\alpha = \frac{R - \delta R}{2R} = \frac{L_0^4 \delta B}{6B_s R}. \quad (4)$$

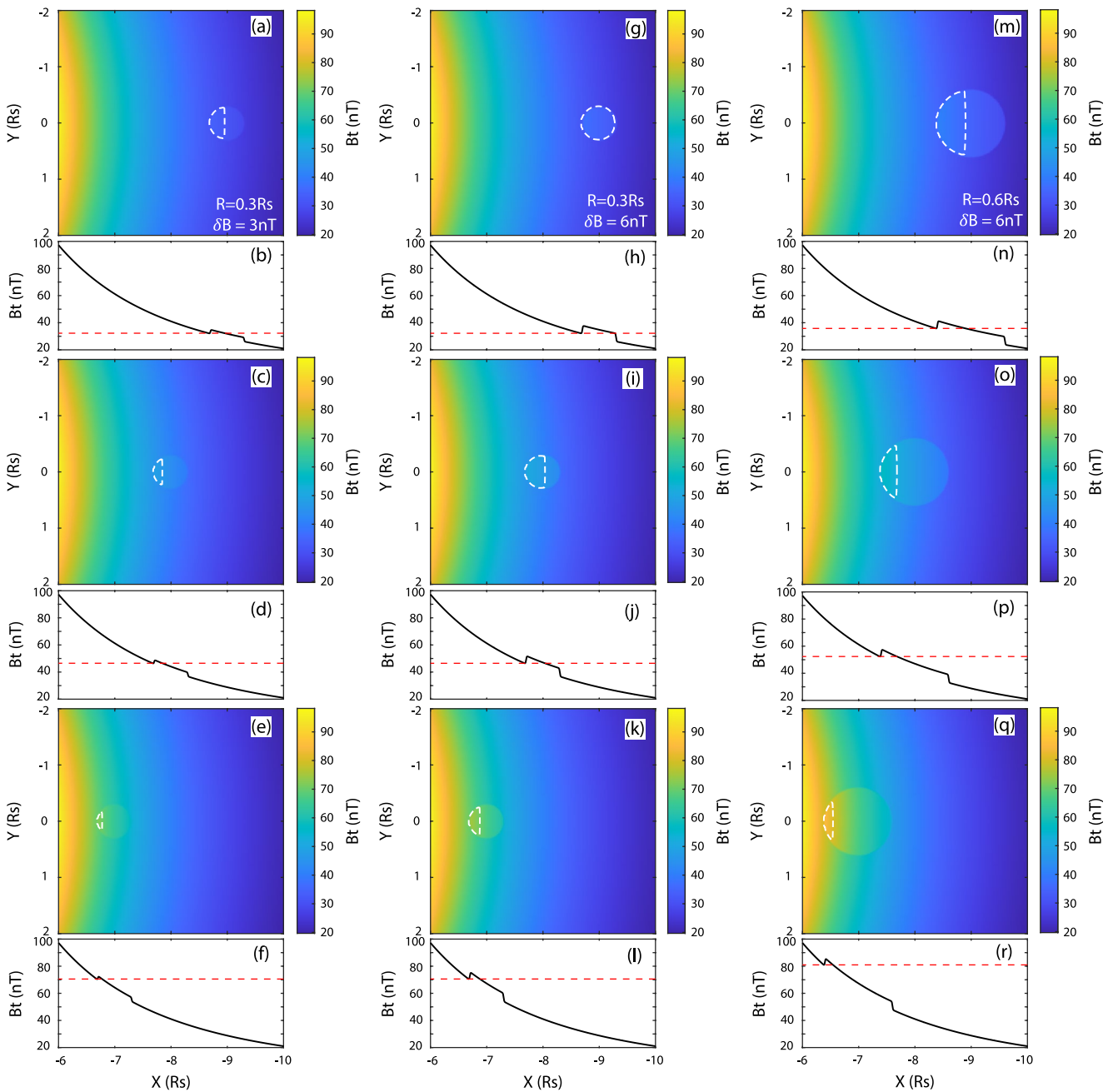


**Figure 3.** Variations of the trapping region under different parameters. (a) Equatorial distribution of the magnetic strength (background color), with an injection flux tube centering at  $L_0 = 9$ . The field enhancement  $\delta B$  and the flux-tube radius  $R$  are 3 nT and  $0.3R_s$ , respectively, as given in the lower-right corner. (b) Radial profile of the field strength at  $y = 0$ , based on same parameters as in panel (a). The horizontal red line represents the contour value at panel (a). Panels (c)–(d) and (e)–(f) are in the same format as (a)–(b), except that the flux-tube center is at  $L_0 = 8$  and  $L_0 = 7$ , respectively. The middle and right columns are in the same format as the left column, except that they apply to different parameters in the lower-right corner in panels (g) and (m).

Obviously, a larger central L-shell, a stronger field enhancement, and a smaller flux-tube radius would lead to a larger portion of the trapping region within the tube.

Figure 3 shows the extent of the trapping region under different flux-tube parameters. We first set the flux-tube center  $L_0 = 9$ , the field enhancement  $\delta B = 6$  nT, and the tube radius  $R = 0.3R_s$ . According to Equation 4, these parameters correspond to  $\alpha \sim 1$ . The field-strength distribution is shown in Figure 3g, with the white contour indicating the full occupation of the flux tube by the trapping region. Figure 3h shows the 1D field-strength profile along the  $y = 0$  axis. In this case, any traversing spacecraft would observe dispersionless features for



perpendicular-moving particles and energy-dispersive signatures for bouncing particles (like the observations for Case I, see Figure 1). Since  $\alpha$  is proportional to  $L_0^4$ , a flux tube with the same parameters except for a lower L-shell would have a smaller trapping region (see the reduced extent for  $L_0 = 8$  in Figures 3i and 3j, and more significantly for  $L_0 = 7$  in Figures 3k and 3l). The effects of field enhancement  $\delta B$  and tube radius  $R$  are shown in Figures 3a–3f and 3m–3r, respectively. The results, consistent with predictions in Equation 4, demonstrate the shrinkage of the trapping region (and consequently, the increasing likelihood of pitch-angle dependent observations as in Case II) with weaker field perturbations and/or larger tube radius. In other words, even if we focus on a single flux tube, different observational features (Case I-like or Case II-like) could be expected at different stages of its evolution. Note that although the parameters in Figure 3 are given arbitrarily, their selection in reality must be constrained by the pressure-balance requirement. For example, the field perturbations in the inner magnetosphere with lower plasma beta values are usually weaker (Sergis et al., 2010).

#### 4. Summary and Discussions

We utilize Cassini observations to understand the motion of energetic particles within injection flux tubes of Saturn's magnetosphere. The diverse features of perpendicular-moving and bouncing particles reveal the following:

1. The sharp magnetic gradient at the flux-tube edges results in closed contours of the field strength, which enables closed drift trajectories of perpendicular-moving particles within the trapping region.
2. The bouncing particles are less affected by the sharp gradient, and therefore drift at their energy-dependent velocities to form the characteristic energy-dispersion and particle-leakage signatures.
3. The diverse observational signatures of energetic particles within the injection flux tubes depend on particle pitch angles, spacecraft traversal paths, and trapping regions. The extent of the trapping region to the entire flux tube depends on the flux tube's size, center L-shell, and associated magnetic enhancements.

Based on the event lists of Azari et al. (2018), Lai et al. (2016), and Paranicas et al. (2020), we also carry out a survey of injection flux tubes with sharp magnetic gradients near the edges. To examine the particle dispersion properties, we impose requirements on pitch-angle coverage (at least one of the CHEMS telescopes has the field-of-view centered near  $90^\circ$ ) and observational data points (at least three within the flux tube), which significantly reduces the number of events. Among these flux tubes, four events are categorized into Case-I type (with energy-dispersive and dispersionless features for bouncing and perpendicular-moving particles, respectively), and five events are Case-II type (energy-dispersive for both bouncing and perpendicular-moving particles).

Ideally, one may expect another kind of observational signatures (in addition to the two types shown above) when the spacecraft enters the flux tube within the trapping region and departs at locations outside. In this case, the spacecraft is expected to observe Case I-like features during its stay in the trapping region, and Case II-like features afterward. However, we fail to identify a single event with such combined signatures. This may provide further constraints on flux-tube properties. Since a spacecraft with a larger radial velocity (in the flux-tube rest frame) would more likely traverse both the trapping and leaking regions, the observational scarcity of the combined signatures may indicate that the radially-inward velocities of the injection flux tubes are low in general. An alternative explanation is that the particle trapping may be less efficient for flux tubes with larger radially-inward velocities, since in these cases the stronger electric field could perturb the drift motion of the trapped particles. Future studies are required to quantitatively examine the role of the electric field on particle dynamics within injection flux tubes.

Our results also provide important constraints to the efforts of determining the starting positions and ages of the injection flux tubes. Caution should be applied when tracing the perpendicular-moving particles backward to the starting position, especially if we consider the larger coverage of the trapping region at higher L-shells. In the backward tracing approach (e.g., Lai et al., 2021), the particle arrival at the flux-tube edge is treated as the end of the tracing procedure; but this is not necessarily true for perpendicular-moving particles since they may follow closed trajectories around the trapping region. In this sense, the bouncing particles would be better candidates in the determination of flux-tube ages and starting points.

Moreover, the particle distributions within the flux tubes could be modified by the trapping of perpendicular-moving particles and the leakage of bouncing particles, which could enhance the temperature anisotropy therein and contribute to the excitation of various plasma waves. This is supported by observations of electrostatic cyclotron

harmonics and whistle-mode chorus waves in localized flux tubes (Menietti et al., 2008). The trapping process could also apply to similar flux tubes in Jupiter's magnetosphere (e.g., Thorne et al., 1997), where localized chorus emissions have also been reported (Menietti et al., 2021). Therefore, it would be interesting to study the relationship between particle trapping and plasma wave excitation within injection flux tubes at the magnetospheres of giant planets.

### Data Availability Statement

The observational data from Cassini is accessible at the Planetary Plasma Interactions (PPI) Node of the Planetary Data System (PDS) (<https://pds-ppi.igpp.ucla.edu/mission/Cassini-Huygens>), in which the 1-s cadence magnetic field measurements are obtained from Dougherty et al. (2019), the CHEMS measurement are available at Vandegriff et al. (2018), and the CAPS-ELS data are provided by Waite and Wilson (2022).

### References

- André, N., Dougherty, M. K., Russell, C. T., Leisner, J. S., & Khurana, K. K. (2005). Dynamics of the Saturnian inner magnetosphere: First inferences from the Cassini magnetometers about small-scale plasma transport in the magnetosphere. *Geophysical Research Letters*, 32(14), L14S06. <https://doi.org/10.1029/2005GL022643>
- André, N., Persoon, A. M., Goldstein, J., Burch, J. L., Louarn, P., Lewis, G. R., et al. (2007). Magnetic signatures of plasma-depleted flux tubes in the Saturnian inner magnetosphere. *Geophysical Research Letters*, 34(14), L14108. <https://doi.org/10.1029/2007GL030374>
- Azari, A. R., Liemohn, M. W., Jia, X., Thomsen, M. F., Mitchell, D. G., Sergis, N., et al. (2018). Interchange Injections at Saturn: Statistical survey of energetic H<sup>+</sup> sudden flux intensifications. *Journal of Geophysical Research: Space Physics*, 123(6), 4692–4711. <https://doi.org/10.1029/2018JA025391>
- Baumjohann, W., & Treumann, R. A. (1996). *Basic space plasma physics*. Published by Imperial College Press and Distributed by World Scientific Publishing Co.
- Blanc, M., Andrews, D. J., Coates, A. J., Hamilton, D. C., Jackman, C. M., Jia, X., et al. (2015). Saturn plasma sources and associated transport processes. *Space Science Reviews*, 192(1), 237–283. <https://doi.org/10.1007/s11214-015-0172-9>
- Burch, J. L., Goldstein, J., Hill, T. W., Young, D. T., Crary, F. J., Coates, A. J., et al. (2005). Properties of local plasma injections in Saturn's magnetosphere. *Geophysical Research Letters*, 32(14), L14S02. <https://doi.org/10.1029/2005GL022611>
- Chen, Y., & Hill, T. W. (2008). Statistical analysis of injection/dispersion events in Saturn's inner magnetosphere. *Journal of Geophysical Research*, 113(A7), A07215. <https://doi.org/10.1029/2008JA013166>
- Delamere, P. A., Otto, A., Ma, X., Bagenal, F., & Wilson, R. J. (2015). Magnetic flux circulation in the rotationally driven giant magnetospheres. *Journal of Geophysical Research: Space Physics*, 120(6), 4229–4245. <https://doi.org/10.1002/2015JA021036>
- Dougherty, M. K., Kellock, S., Slootweg, A. P., Achilleos, N., Joy, S. P., & Mafi, J. N. (2019). Cassini orbiter MAG calibrated summary 1 SEC averages V2.0, CO-E/SW/J/S-MAG-4-SUMM-1SECAVG-V2.0 [Dataset]. NASA Planetary Data System. <https://doi.org/10.17189/1519603>
- Dougherty, M. K., Kellock, S., Southwood, D. J., Balogh, A., Smith, E. J., Tsurutani, B. T., et al. (2004). The Cassini magnetic field investigation. *Space Science Reviews*, 114(1), 331–383. <https://doi.org/10.1007/s11214-004-1432-2>
- Guo, R. L., Yao, Z. H., Wei, Y., Ray, L. C., Rae, I. J., Arridge, C. S., et al. (2018). Rotationally driven magnetic reconnection in Saturn's dayside. *Nature Astronomy*, 2(8), 640–645. <https://doi.org/10.1038/s41550-018-0461-9>
- Hill, T. W., Rymer, A. M., Burch, J. L., Crary, F. J., Young, D. T., Thomsen, M. F., et al. (2005). Evidence for rotationally driven plasma transport in Saturn's magnetosphere. *Geophysical Research Letters*, 32(14), L14S10. <https://doi.org/10.1029/2005GL022620>
- Krimigis, S. M., Mitchell, D. G., Hamilton, D. C., Livi, S., Dandouras, J., Jaskulek, S., et al. (2004). Magnetosphere imaging instrument (MIMI) on the Cassini mission to Saturn/Titan. *Space Science Reviews*, 114(1), 233–329. <https://doi.org/10.1007/s11214-004-1410-8>
- Lai, H. R., Jia, Y.-D., Russell, C. T., Jia, X., Masters, A., Dougherty, M. K., & Cui, J. (2021). Magnetic flux circulation in the Saturnian magnetosphere as constrained by Cassini observations in the inner magnetosphere. *Journal of Geophysical Research: Space Physics*, 126(11), e2021JA029304. <https://doi.org/10.1029/2021JA029304>
- Lai, H. R., Russell, C. T., Jia, Y. D., Wei, H. Y., & Dougherty, M. K. (2016). Transport of magnetic flux and mass in Saturn's inner magnetosphere. *Journal of Geophysical Research: Space Physics*, 121(4), 3050–3057. <https://doi.org/10.1002/2016JA022436>
- Linder, D. R., Coates, A. J., Woodliffe, R. D., Alsop, C., Johnstone, A. D., Grande, M., et al. (1998). The Cassini CAPS electron spectrometer. In *Measurement techniques in space plasmas: Particles* (pp. 257–262).
- Liu, X., Hill, T. W., Wolf, R. A., Sazykin, S., Spiro, R. W., & Wu, H. (2010). Numerical simulation of plasma transport in Saturn's inner magnetosphere using the Rice Convection Model. *Journal of Geophysical Research*, 115(A12), A12254. <https://doi.org/10.1029/2010JA015859>
- Mauk, B. H., Hamilton, D. C., Hill, T. W., Hospodarsky, G. B., Johnson, R. E., Paranicas, C., et al. (2009). Fundamental plasma processes in Saturn's magnetosphere. In M. K. Dougherty, L. W. Esposito, & S. M. Krimigis (Eds.), *Saturn from Cassini-Huygens* (pp. 281–331). Springer Netherlands.
- Menietti, J. D., Averkamp, T. F., Imai, M., Kurth, W. S., Clark, G. B., Allegrini, F., et al. (2021). Low-latitude whistler-mode and higher-latitude z-mode emission at Jupiter observed by Juno. *Journal of Geophysical Research: Space Physics*, 126(2), e2020JA028742. <https://doi.org/10.1029/2020JA028742>
- Menietti, J. D., Santolik, O., Rymer, A. M., Hospodarsky, G. B., Persoon, A. M., Gurnett, D. A., et al. (2008). Analysis of plasma waves observed within local plasma injections seen in Saturn's magnetosphere. *Journal of Geophysical Research*, 113(A5), A05213. <https://doi.org/10.1029/2007JA012856>
- Mitchell, D. G., Brandt, P. C., Carbary, J. F., Kurth, W. S., Krimigis, S. M., Paranicas, C., et al. (2015). Injection, interchange, and reconnection. In *Magnetotails in the solar system* (pp. 327–343).
- Paranicas, C., Thomsen, M. F., Achilleos, N., Andriopoulou, M., Badman, S. V., Hospodarsky, G., et al. (2016). Effects of radial motion on interchange injections at Saturn. *Icarus*, 264, 342–351. <https://doi.org/10.1016/j.icarus.2015.10.002>
- Paranicas, C., Thomsen, M. F., Kollmann, P., Azari, A. R., Bader, A., Badman, S. V., et al. (2020). Inflow speed analysis of interchange injections in Saturn's magnetosphere. *Journal of Geophysical Research: Space Physics*, 125(9), e2020JA028299. <https://doi.org/10.1029/2020JA028299>

### Acknowledgments

This work was supported by NSFC Grant 42174184 and China Postdoctoral Science Foundation Grant 2023M730035.

- Rymer, A. M., Mauk, B. H., Hill, T. W., André, N., Mitchell, D. G., Paranicas, C., et al. (2009). Cassini evidence for rapid interchange transport at Saturn. *Planetary and Space Science*, 57(14), 1779–1784. <https://doi.org/10.1016/j.pss.2009.04.010>
- Sergis, N., Krimigis, S. M., Roelof, E. C., Arridge, C. S., Rymer, A. M., Mitchell, D. G., et al. (2010). Particle pressure, inertial force, and ring current density profiles in the magnetosphere of Saturn, based on Cassini measurements. *Geophysical Research Letters*, 37(2), L02102. <https://doi.org/10.1029/2009GL041920>
- Sonnerup, B. U. Ö., & Scheible, M. (1998). Minimum and maximum variance analysis. *ISSI Scientific Reports Series, 1*, 185–220.
- Thomsen, M. F. (2013). Saturn's magnetospheric dynamics. *Geophysical Research Letters*, 40(20), 5337–5344. <https://doi.org/10.1002/2013GL057967>
- Thomsen, M. F., & Coates, A. J. (2019). Saturn's plasmopause: Signature of magnetospheric dynamics. *Journal of Geophysical Research: Space Physics*, 124(11), 8804–8813. <https://doi.org/10.1029/2019JA027075>
- Thomsen, M. F., Mitchell, D. G., Jia, X., Jackman, C. M., Hospodarsky, G., & Coates, A. J. (2015). Plasmopause formation at Saturn. *Journal of Geophysical Research: Space Physics*, 120(4), 2571–2583. <https://doi.org/10.1002/2015JA021008>
- Thorne, R. M., Armstrong, T. P., Stone, S., Williams, D. J., McEntire, R. W., Bolton, S. J., et al. (1997). Galileo evidence for rapid interchange transport in the Io torus. *Geophysical Research Letters*, 24(17), 2131–2134. <https://doi.org/10.1029/97GL01788>
- Vandegriff, J., Kusterer, M. B., & Mafi, J. (2018). CO-S-MIMI-4-CHEMS-CALIB-V1.0, CASSINI S MIMI CHEMS sensor calibrated data V1.0 [Dataset]. NASA Planetary Data System. <https://doi.org/10.17189/1519606>
- Vasyliunas, V. M. (1983). Plasma distribution and flow. In A. J. Dessler (Ed.), *Physics of the Jovian magnetosphere* (pp. 395–453). Cambridge University Press.
- Waite, J. H., & Wilson, R. J. (2022). Cassini-Huygens plasma spectrometer (CAPS) calibrated electron spectrometer data collection [Dataset]. NASA Planetary Data System. <https://doi.org/10.17189/fj9-4740>
- Wilson, R. J., Tokar, R. L., & Henderson, M. G. (2009). Thermal ion flow in Saturn's inner magnetosphere measured by the Cassini plasma spectrometer: A signature of the Enceladus torus? *Geophysical Research Letters*, 36(23), L23104. <https://doi.org/10.1029/2009GL040225>
- Yao, Z. H., Coates, A. J., Ray, L. C., Rae, I. J., Grodent, D., Jones, G. H., et al. (2017). Corotating magnetic reconnection site in Saturn's magnetosphere. *The Astrophysical Journal Letters*, 846(2), L25. <https://doi.org/10.3847/2041-8213/aa88af>
- Yin, Z.-F., Zhou, X.-Z., Hu, Z.-J., Yue, C., Zong, Q.-G., Hao, Y.-X., et al. (2022). Localized excitation of electromagnetic ion cyclotron waves from anisotropic protons filtered by magnetic dips. *Journal of Geophysical Research: Space Physics*, 127(6), e2022JA030531. <https://doi.org/10.1029/2022JA030531>
- Yin, Z.-F., Zhou, X.-Z., Zong, Q.-G., Liu, Z.-Y., Yue, C., Xiong, Y., et al. (2021). Inner magnetospheric magnetic dips and energetic protons trapped therein: Multi-spacecraft observations and simulations. *Geophysical Research Letters*, 48(7), e2021GL092567. <https://doi.org/10.1029/2021GL092567>
- Young, D. T., Berthelier, J. J., Blanc, M., Burch, J. L., Coates, A. J., Goldstein, R., et al. (2004). Cassini plasma spectrometer investigation. *Space Science Reviews*, 114(1), 1–112. <https://doi.org/10.1007/s11214-004-1406-4>
- Zhou, X.-Z., Angelopoulos, V., Liu, J., Runov, A., & Li, S. S. (2014). On the origin of pressure and magnetic perturbations ahead of dipolarization fronts. *Journal of Geophysical Research: Space Physics*, 119(1), 211–220. <https://doi.org/10.1002/2013JA019394>